Check for updates

Layered Si$_2$Te$_3$-based anodes for high-performance Li-ion batteries†

Byeong Guk Kim,‡[ac] Jihyeon Ryu, [ID] ‡[bc] Dong Gyun Hong,[ac] Kyungmin Do,[bc] Sooyeon Jeong,[a] Hye Jung Lee,[a] Seung Yol Jeong,*[ac] Sunhye Yang*[bc] and Ki-Hun Nam [ID] *[bc]

We develop a scalable solid-state synthesis for Si$_2$Te$_3$ and its carbon composite (Si$_2$Te$_3$@C) to address the challenges of silicon-based anodes in lithium-ion batteries (LIBs). The Si$_2$Te$_3$@C composite exhibits enhanced electrochemical performance, including high reversible capacity, excellent cycling stability, and improved rate capability, positioning it as a promising candidate for high-performance LIB anodes.

Layered materials, characterized by strong in-plane covalent bonding and weak out-of-plane van der Waals (vdW) inter-actions, have garnered significant interest due to their unique physical and chemical properties.[1–3] These materials, including graphite, black phosphorus, transition metal chalcogenides (TMCs), and MXenes, allow for the intercalation of foreign atoms or molecules between layers, making them attractive as electrode materials for lithium-ion batteries (LIBs). Notably, graphite serves as a representative anode material due to its reversible Li-ion intercalation mechanism, while other layered materials, such as phosphides, chalcogenides, carbides, and nitrides, are actively studied for their high capacity and structural advantages, positioning them as promising alternatives for next-generation LIB electrodes.[4–7]

Silicon (Si) has been widely recognized as a promising anode material for LIBs due to its abundance, low redox potential (0.2–0.3 V *vs.* Li$^+$/Li), and exceptionally high theoretical capacity (3578 mA h g^{-1} for Li$_{3.75}$Si at room temperature).[8] However, Si-based anodes suffer from severe structural degradation caused by 300–400% volume expansion during lithiation/delithiation processes.[9]

This dramatic volume change leads to the mechanical fracture of particles, electrical disconnection of active materials, and the formation of dynamic interfaces at the electrode–electrolyte boundary. Such dynamic interfaces not only degrade electrical contact but also promote undesirable side reactions with the electrolyte, resulting in the continuous growth of the solid electrolyte interphase (SEI) layer, ultimately causing capacity fading and poor cycle life.[10] To address these intrinsic limitations of Si anodes, extensive efforts have been devoted to improving their performance through various strategies, including carbon coatings, composite structures, size and morphology control, and the development of Si-alloys and Si-compounds.[11–14] Among these approaches, Si-alloys and Si-compounds have emerged as particularly promising solutions due to their structural stability and distinct Li-storage mechanisms, which effectively mitigate the effects of volume expansion and improve cycling performance.

Recently, Si$_2$Te$_3$, a two-dimensional (2D) silicon-based chalcogenide, has attracted considerable attention as a high-performance material for energy storage applications. It exhibits excellent environmental stability, a strain-dependent bandgap, and a high Seebeck coefficient, making it highly versatile.[15,16] Its trigonal layered crystal structure with a stoichiometric ratio of Si/Te = 2/3 supports the formation of natural structural defects through the partial absence of Si–Si pairs, resulting in p-type behavior and enhanced light–matter interactions.[17] These features contribute to improved photoelectric conversion efficiency and a broad photoresponse range, making it suitable for optoelectronic devices as well. Furthermore, the layered structure of Si$_2$Te$_3$ provides large interlayer spacing, which facilitates lithium-ion diffusion during lithiation/delithiation processes, addressing the volume expansion issue associated with conventional Si anodes. Its indirect bandgap nature and photoelectronic properties further expand its potential applications beyond energy storage, particularly in optoelectronics. Despite its promising structural and electronic properties, the scalable synthesis of Si$_2$Te$_3$ remains a challenge. Therefore, developing simple and cost-effective methods for producing Si$_2$Te$_3$ is crucial to fully realize its potential as a high-performance anode material in LIBs.

[a] *Nano Hybrid Technology Research Center, Korea Electrotechnology Research Institute (KERI), Changwon, 51543, Republic of Korea. E-mail: syjeong@keri.re.kr*

[b] *Battery Research Division, Korea Electrotechnology Research Institute (KERI), Changwon, 51543, Republic of Korea. E-mail: shyang@keri.re.kr, khnam@keri.re.kr*

[c] *Electric Energy Materials Engineering, KERI School, University of Science and Technology (UST), Daejeon, 34113, Republic of Korea*

† Electronic supplementary information (ESI) available. See DOI: https://doi.org/10.1039/d5cc00437c

‡ Byeong Guk Kim and Jihyeon Ryu contributed equally to this work.

In this study, we present a facile and scalable approach for synthesizing layered Si_2Te_3 through a solid-state process that combines sequential ball-milling (BM) and heat-treatment (HT). While Si_2Te_3 exhibits a unique atomic arrangement, its electrochemical performance is largely influenced by its intrinsic properties. To overcome its inherent low electrical conductivity, a composite structure incorporating amorphous carbon is developed. The Li-storage properties of this composite are further evaluated, demonstrating its potential as a high-performance Si-based anode for LIBs. Moreover, its Li-storage mechanism is systematically analyzed using *ex situ* X-ray diffraction (XRD) and high-resolution transmission electron microscopy (HR-TEM) based on the dQ/dV plots. This work provides a comprehensive understanding of the electrochemical behavior of Si_2Te_3-based composites and offers useful design strategies for next-generation LIB anodes.

Silicon–tellurium (Si–Te) compounds are primarily known to form two distinct phases, $SiTe_2$ and Si_2Te_3.[17,18] However, the Si–Te phase diagram identifies Si_2Te_3 as the only thermodynamically stable compound in this system (Fig. S1, ESI†). Si_2Te_3 crystallizes in a hexagonal structure with a $P\bar{3}1c$ (no. 163) space group and exhibits lattice parameters of $a = b = 7.4$ Å and $c = 13.5$ Å. It features a layered crystal structure with each layer having a thickness of 6.7 Å. The layers consist of two parallel planes of tellurium atoms, with Si–Si dimers occupying the interlayer regions.[17] The interlayer spacing in Si_2Te_3 is approximately 3.2 Å, which is comparable to well-known layered materials such as graphene ($\sim$3.4 Å), black phosphorus ($\sim$3.2 Å), and MoS_2 ($\sim$3.2 Å). This relatively large interlayer spacing facilitates rapid diffusion and reversible accommodation of Li-ions, making Si_2Te_3 a promising candidate for LIB anode materials.

Si_2Te_3 was synthesized *via* a solid-state reaction involving sequential BM and HT processes. The XRD patterns of the synthesized Si_2Te_3 matched well with those of the hexagonal Si_2Te_3 phase (JCPDS #75-0820), confirming that the material was formed homogeneously without impurity phases (Fig. 1a and Fig. S2, ESI†). To further investigate its structural properties, the XRD pattern was refined using the Rietveld method (Fig. 1b). The corresponding lattice parameters–$\chi^2 = 1.01$, $R_p = 15.5\%$, and $R_{wp} = 19.1\%$ (Table S1, ESI†)—showed excellent agreement with experimental data, indicating the high crystallinity of the synthesized material. The morphology and particle size distribution of Si_2Te_3 were examined using scanning electron microscopy (SEM) and particle size analysis (PSA). As shown in Fig. S3 (ESI†), the average particle size was approximately 10.01 μm, with irregular particle morphologies. To further validate the homogeneous synthesis, Raman spectroscopy and HR-TEM analyses were conducted. The Raman spectra exhibited three distinct peaks at 139, 291, and 504 cm^{-1}, which were clearly distinguishable from those of Si and Te (Fig. S4, ESI†), confirming the formation of the Si_2Te_3 phase. Additionally, HR-TEM images (Fig. S5, ESI†) revealed well-developed Si_2Te_3 crystallites with clearly visible diffraction patterns (DPs) corresponding to the hexagonal structure. The observed crystal planes, including ($\bar{1}\bar{1}4$), (110), ($\bar{1}\bar{1}2$), and ($\bar{1}\bar{1}6$), matched the main peaks detected in the XRD patterns, further
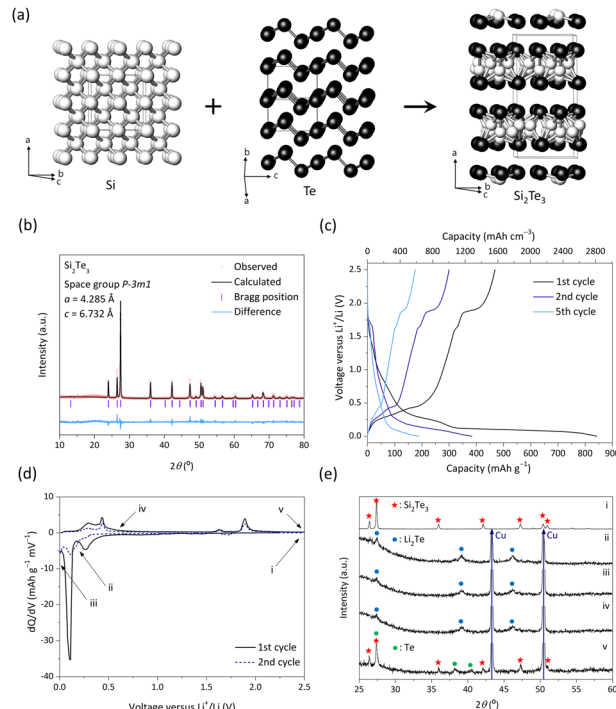

Fig. 1 (a) Crystal structure of layered Si_2Te_3; (b) Rietveld-refined XRD patterns of Si_2Te_3; (c) GDC profiles of Si_2Te_3 anode at 100 mA g^{-1}; (d) dQ/dV plots for Si_2Te_3; (e) *ex situ* XRD patterns of Si_2Te_3 anode during first cycle.

verifying the structural integrity and high crystalline quality of the synthesized Si_2Te_3.

To evaluate the electrochemical Li-storage properties of the Si_2Te_3 anode, galvanostatic discharge and charge (GDC) profiles were recorded at a current density of 100 mA g^{-1} (Fig. 1c). For comparison, Si and Te anodes were also prepared and tested electrochemically using bulk Si and Te powders. The Si anode exhibited a high initial lithiation/delithiation capacity of 3511/1925 mA h g^{-1} (Fig. S6, ESI†). However, its capacity rapidly degraded to 282 mA h g^{-1} after 10 cycles due to severe volume expansion ($>$300%) caused by the alloying/dealloying reactions with Li_xSi phases. In contrast, the Te anode demonstrated a lower lithiation/delithiation capacity of 199/133 mA h g^{-1} and suffered from poor capacity retention due to its low electrical conductivity. Compared to these materials, the Si_2Te_3 anode exhibited an initial lithiation/delithiation capacity of 843/468 mA h g^{-1} (2816/1563 mA g cm^{-3}) with an ICE of 55.5%. Thus, Li-storage performance of Si_2Te_3 is also not sufficient to meet the criteria for high-performance LIB anodes compared with Si-based anodes.

To analyze the Li-storage mechanism of the Si_2Te_3 anode, *ex situ* XRD analysis was performed based on the dQ/dV plot. The dQ/dV plot exhibited two prominent peaks during the discharge process and three peaks during the charge process (Fig. 1d). *Ex situ* XRD analysis (Fig. 1e) revealed that as the potential decreased from open circuit potential (i) to 0.17 V (ii), the Si_2Te_3 phase disappeared, and only the Li_2Te phase (JCPDS #77-2147) was detected, confirming the conversion reaction of Si_2Te_3 into Li_2Te and amorphous Si. Further analysis

at 0 V (iii) revealed that the Li$_2$Te phase remained. To verify the formation of the Li–Si phase after full lithiation, the dQ/dV plots for Si and Si$_2$Te$_3$ anodes were compared (Fig. S7, ESI†).[19] The overlapping peak positions confirmed that the formation of the Li$_{3.75}$Si phase was consistent in both anodes. Upon charging to 0.6 V (iv), the Li$_2$Te phase persisted, suggesting partial recombination during the initial charging process. At the fully charged state (2.5 V, v), the Si$_2$Te$_3$ phase reappeared. However, the Te phase was also detected, indicating that the Si$_2$Te$_3$ phase was partially recombined, with residual Te and amorphous Si coexisting. These results demonstrate that the Si$_2$Te$_3$ anode undergoes a reversible conversion reaction, although the presence of residual Te and amorphous Si suggests partial phase reconstruction during the charging process.

To further enhance the Li-reversibility and reactivity of Si$_2$Te$_3$, we designed a Si$_2$Te$_3$@C composite by combining the as-synthesized Si$_2$Te$_3$ with carbon black using a BM process. Carbon-supported composites are well-known to improve ionic and electronic conductivity, accommodate large volume changes, and suppress the agglomeration of nanoscale Li-active materials during repeated cycling.[20,21] The introduction of conductive carbon matrices not only facilitates charge transfer kinetics but also stabilizes the structural integrity of the Si$_2$Te$_3$ particles, enabling prolonged cycle life and rate performance. The XRD pattern of the Si$_2$Te$_3$@C composite revealed broadened diffraction peaks, indicating a reduction in crystallinity during the composite formation process (Fig. S8, ESI†). This suggests that the BM process induced a partial amorphization of the material, which could contribute to enhanced electrochemical properties by providing shorter diffusion paths for Li ions. HR-TEM analysis further confirmed that the synthesized Si$_2$Te$_3$@C composite consists of ultrafine nanocrystallites ($\sim$5–7 nm) uniformly embedded within an amorphous carbon matrix (Fig. 2a–c). The DPs obtained from selected area electron diffraction (SAED) matched well with the hexagonal crystal structure of Si$_2$Te$_3$, supporting the structural stability of the nanocrystallites within the composite. Energy-dispersive X-ray spectroscopy (EDS) mapping derived from scanning TEM (STEM) images verified the homogeneous distribution of elemental Si (yellow) and Te (green) throughout the carbon matrix (blue), highlighting the well-mixed composition of the composite. In addition, the average particle size of Si$_2$Te$_3$@C was approximately 6.8 μm, with irregular particle morphologies (Fig. S9, ESI†).

Fig. 2d shows the GDC profiles of the Si$_2$Te$_3$@C anode at a current density of 100 mA g^{-1}. The initial lithiation/delithiation capacities were 816 mA h g^{-1} (1746 mA h cm^{-3}) and 559 mA h g^{-1} (1196 mA h cm^{-3}), respectively. Considering the first irreversible capacity of the carbon component (30 wt%, 110 mA h g^{-1}, Fig. S10, ESI†), the Si$_2$Te$_3$@C composite exhibited significantly improved Li reversibility and reactivity compared to the pristine Si$_2$Te$_3$ anode. In addition, electrochemical impedance spectroscopy (EIS) and the corresponding Nyquist plots were analyzed (Fig. S11, ESI†). The charge transfer resistance (R_{ct}) of the Si$_2$Te$_3$@C nanocomposite anode was measured as 34.9 Ω, which is significantly lower than that of the pristine Si$_2$Te$_3$ anode (59.7 Ω). Furthermore, the nanocomposite exhibited a higher Li-ion diffusion coefficient of 1.23×10^{-15} cm^2 s^{-1}, compared to 1.11×10^{-14} cm^2 s^{-1} for the
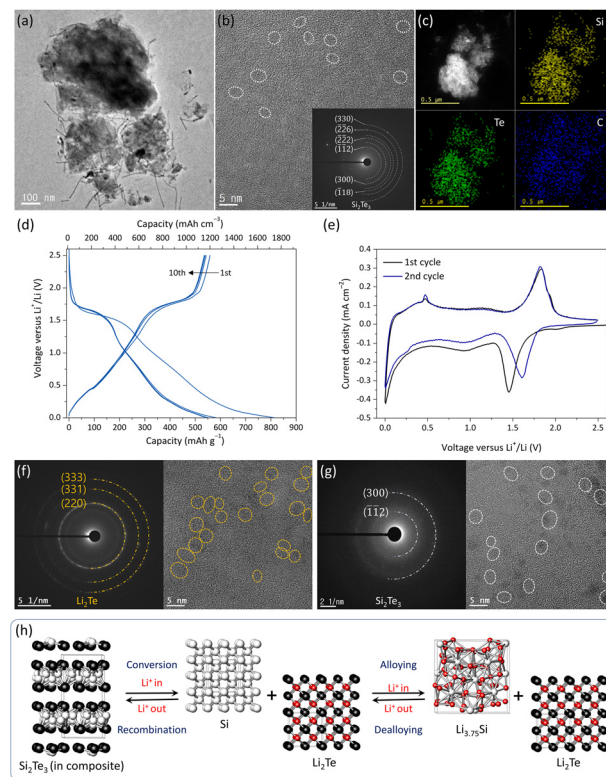

Fig. 2 (a) Bright field TEM image, (b) HR-TEM image with corresponding DPs and, (c) STEM image with corresponding EDS mapping images of Si$_2$Te$_3$@C; (d) GDC profiles of Si$_2$Te$_3$@C at 100 mA g^{-1}; (e) CV plots of Si$_2$Te$_3$@C; ex situ HR-TEM images with corresponding DPs of Si$_2$Te$_3$@C after (f) full discharged potential (0 V) and (g) full charged potential (2.5 V); (h) schematic of the crystallographic phase change mechanism of Si$_2$Te$_3$@C.

pristine Si$_2$Te$_3$, as calculated from the Z_{re}-angular frequency ($\omega^{-1/2}$) relationship in the low-frequency region.

To investigate the Li-storage mechanism, ex situ XRD analysis was performed at selected potentials based on the dQ/dV plot and cyclic voltammetry (CV) results. The CV plot displayed two distinct peaks during Li insertion/extraction, suggesting a conversion-type reaction mechanism (Fig. 2e). Although XRD patterns were collected at five cut-off potential points, all patterns exhibited an amorphous nature, likely due to the low crystallinity of Si$_2$Te$_3$ within the composite (Fig. S12, ESI†). Thus, to investigate the structural changes of Si$_2$Te$_3$@C, ex situ HR-TEM analysis is performed and the results are shown in Fig. 2f and g. At the fully discharged potential (0 V), well-dispersed nanocrystallites of Li$_2$Te (5–8 nm) and amorphous Li$_{3.75}$Si phases were observed, confirming that Si$_2$Te$_3$ was fully converted into these phases during the discharge process (Fig. 2f). In contrast, at the fully charged potential (2.5 V), only the Si$_2$Te$_3$ phase was detected, indicating that Li$_{3.75}$Si and Li$_2$Te recombined to reform Si$_2$Te$_3$ with 5–7 nm nanocrystallites during the charging process (Fig. 2g and h).

These findings confirm that the Si$_2$Te$_3$@C nanocomposite undergoes a reversible conversion reaction, where the Li-storage process is facilitated by the conducting carbon matrix. The carbon matrix not only improves electronic conductivity but also provides structural stability, effectively buffering the
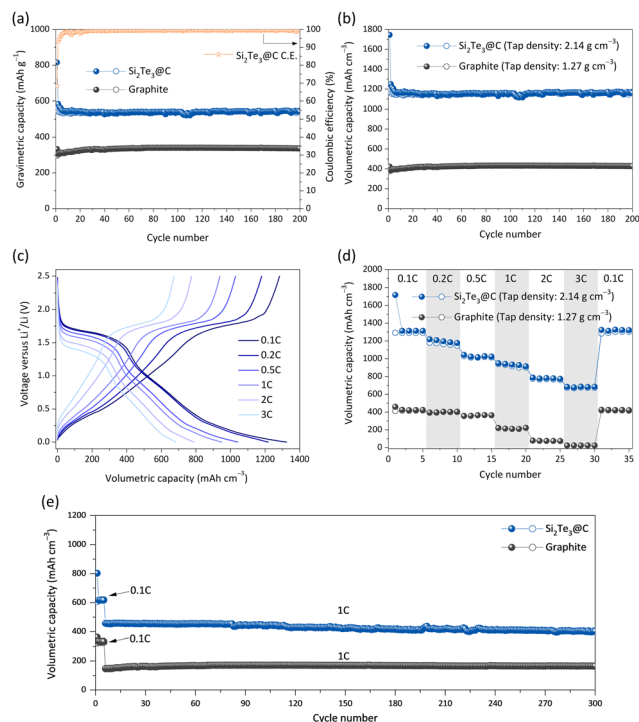
Fig. 3 (a) Gravimetric and (b) volumetric capacities *vs.* cycle number for Si_2Te_3@C and graphite anodes at 100 mA g^{-1}; (c) GDC profiles of Si_2Te_3@C anode at different C-rates (1C: 550 mA g^{-1}); (d) rate capability of Si_2Te_3@C (1C: 550 mA g^{-1}) and graphite (1C: 300 mA g^{-1}) anodes; (e) cycling performance of Si_2Te_3@C (1C: 550 mA g^{-1}) and graphite (1C: 300 mA g^{-1}) anodes at 1C-rate.

volume changes associated with the lithiation/delithiation processes. In addition, the formation of the Li_2Te phase during lithiation, derived from Si_2Te_3 in the composite, could contribute to the electrochemical performance of LIB anodes.[22]

Fig. 3a and b illustrate the electrochemical performance of the Si_2Te_3@C composite anode compared with a commercial graphite anode at a cycling rate of 100 mA g^{-1}. The Si_2Te_3@C composite exhibited a highly reversible gravimetric/volumetric capacity of 816/559 mA h g^{-1} and 1746/1196 mA h cm^{-3}, respectively, which are higher than those of the graphite anode (332/296 mA h g^{-1} and 421/376 mA h cm^{-3}). In addition, the reversible capacity was well-retained after 200 cycles, maintaining approximately 97.3% capacity retention with high Coulombic efficiency per cycle. The rate capability of the Si_2Te_3@C composite anode, as a function of the C-rate (1C = 550 mA g^{-1}), is shown and compared with that of the graphite anode (Fig. 3c, d, and Fig. S13, ESI†). At cycling rates of 0.1, 0.2, 0.5, 1, 2, and 3C, the Si_2Te_3@C composite displayed high reversible capacities of 1291, 1180, 1029, 938, 775, and 672 mA h cm^{-3}, respectively, outperforming the graphite anode. Moreover, during long-term cycling performance of the Si_2Te_3@C composite anode at a cycling rate of 1C (550 mA g^{-1}), the reversible capacity remained at 402 mA h g^{-1} (861 mA h cm^{-3}) with stable capacity retention of 88% after 300 cycles (Fig. 3e). This excellent electrochemical performance can be attributed to the ultrafine Si_2Te_3 nanocrystallites (5–7 nm) embedded within the amorphous carbon support, which effectively provide short Li-ion diffusion paths, enhance ionic and electronic conductivity, and

mitigate the effects of volume expansion during lithiation/delithiation processes (Fig. S14, ESI†).

In summary, this study demonstrates the successful synthesis of layered Si_2Te_3 through a scalable solid-state process combining sequential BM and HT. To address the inherent limitations of Si_2Te_3, including low electrical conductivity and structural instability, a Si_2Te_3@C composite was developed by incorporating amorphous carbon. The carbon matrix effectively enhanced electronic conductivity, provided structural stability, and mitigated volume changes during lithiation/delithiation processes. Electrochemical evaluation revealed that the Si_2Te_3@C composite exhibited high reversible capacities (559 mA h g^{-1}/1196 mA h cm^{-3}) and excellent cycling stability, retaining ∼97.3% of its initial capacity after 200 cycles. It also demonstrated superior rate performance, maintaining ∼402 mA h g^{-1} (861 mA h cm^{-3}) at 1C after 300 cycles with 88% capacity retention. *Ex situ* XRD and HR-TEM analyses confirmed a reversible conversion reaction mechanism involving the formation and recombination of Li_2Te and $Li_{3.75}Si$ phases, facilitated by the conductive carbon matrix. These findings highlight the potential of Si_2Te_3-based composites as high-performance anode materials for next-generation LIBs and provide valuable insights for the design of layered chalcogenide materials with enhanced electrochemical properties.

Data availability

The data supporting this article have been included as part of the ESI.†

Conflicts of interest

There are no conflicts to declare.

Notes and references

1 V. Nicolosi, *et al.*, *Science*, 2013, **340**, 1226419.
2 R. Ma and T. Sasaki, *Adv. Mater.*, 2010, **22**, 5082.
3 M. Naguib, *et al.*, *ACS Nano*, 2012, **6**, 1322.
4 M. Armand and J.-M. Tarascon, *Nature*, 2008, **451**, 652.
5 C.-M. Park and H.-J. Sohn, *Adv. Mater.*, 2007, **19**, 2465.
6 W. Liu, *et al.*, *Energy Storage Mater.*, 2019, **16**, 290.
7 B. Anasori, *et al.*, *Nat. Rev. Mater.*, 2017, **2**, 16098.
8 C.-M. Park, *et al.*, *Chem. Soc. Rev.*, 2010, **39**, 3115.
9 J. Ma, *et al.*, *Adv. Energy Mater.*, 2020, **10**, 1903400.
10 I. Yoon, *et al.*, *ACS Nano*, 2023, **17**, 6943.
11 K.-H. Nam, *et al.*, *J. Mater. Chem. A*, 2023, **11**, 4987.
12 L. Sun, *et al.*, *Energy Storage Mater.*, 2022, **46**, 482.
13 H. Wu and Y. Cui, *Nano Today*, 2012, **7**, 414.
14 X. Zuo, *et al.*, *Nano Energy*, 2017, **31**, 113.
15 V. L. Johnson, *et al.*, *Nano Res.*, 2019, **12**, 2373.
16 M. Wang, *et al.*, *ACS Nano*, 2018, **12**, 6163.
17 J. Chen, *et al.*, *Small*, 2021, **17**, 2006496.
18 R. Bhattarai and X. Shen, *ACS Omega*, 2020, **5**, 16848.
19 B. Key, *et al.*, *J. Am. Chem. Soc.*, 2009, **131**, 9239.
20 K.-H. Nam, *et al.*, *ACS Nano*, 2022, **16**, 13704.
21 Z. Wang, *et al.*, *Nano Energy*, 2024, **121**, 109250.
22 Z. Jiang, *et al.*, *Nano Energy*, 2021, **80**, 105589.